Results in Physics 32 (2022) 105125

Contents lists available at ScienceDirect

Results in Physics

journal homepage: www.elsevier.com/locate/rinp

Polarization-insensitive dual-band response governed by quasi bound states in the continuum for high-performance refractive index sensing

Wenjun Liu [a,b], Zhongzhu Liang [a,b,c,*], Zheng Qin [a,b], Xiaoyan Shi [a,b], Fuming Yang [a,b], Dejia Meng [a,*]

[a] State Key Laboratory of Applied Optics, Changchun Institute of Optics, Fine Mechanics and Physics, Chinese Academy of Sciences, Changchun, Jilin 130033, China
[b] University of Chinese Academy of Sciences, Beijing 100049, China
[c] Center for Advanced Optoelectronic Functional Materials Research and Key Laboratory of UV Light-Emitting Materials and Technology of Ministry of Education, College of Physics, Northeast Normal University, Changchun 130024, China

ARTICLE INFO

Keywords:
Refractive index sensing
All-dielectric metasurface
Polarization-insensitive
Dual-band

ABSTRACT

The introduction of distortions into the metasurfaces with in-plane symmetry offers a possibility to achieve resonances with high quality (Q) factors, but such distortions make the metasurfaces sensitive to the polarization state of the incident light. Here, we propose and numerically demonstrate a polarization-insensitive dual-band refractive index (RI) sensor. In this work, the proposed metasurface is imparted with fourfold symmetry by combining two pairs of asymmetric silicon elliptical nanodisks, allowing it to acquire polarization-insensitive properties to the incident light. Two narrow-band reflection peaks with full width at half maximum (FWHM) of 3.36 nm and 4.53 nm are excited and tailored for RI sensing. Their sensitivities are 2756.67 nm/RIU and 2319.93 nm/RIU, with figure of merit (FOM) values of 820.44 RIU^{-1} and 532.09 RIU^{-1}. This work provides a new approach to realize polarization-independent and high-performance RI sensor devices.

Introduction

Metasurfaces are artificial layered two-dimensional materials with thicknesses less than the wavelength, and are widely studied for their ability to effectively modulate electromagnetic wave properties through rationally designed microstructures [1–5]. There are many potential applications for them, including signal processing [6], imaging recognition [7], laser mode-locking [8], augmented reality [9], structural colors [10], and biochemical sensors. Refractive index (RI) sensors realized utilizing metasurfaces can be applied in agriculture, biomedicine, food detection, and chemical industry [11–14]. Initially, benefiting from the development of the surface plasmon theory, metal-based sensing techniques built on surface plasmon polariton or local surface plasmon resonance were widely explored and applied [15–17]. However, the oscillation of free electrons in metals leads to substantial radiative and ohmic losses, which will increase the resonance linewidth resulting in extremely low FOM and Q-factor. Liu et al. reported the RI sensor with a sensitivity of 588 nm/RIU obtained by etching the H-hole structure on an Au film [18], but the FOM is only 3.8. A dual-band plasma absorber for RI sensing was proposed by Cheng et al. [19] with a sensitivity of 1518 nm/RIU but a FOM of only 16.54. And local heating caused by ohmic losses may also change the composition of the measured substance [20]. In contrast, all-dielectric RI sensors as a prospective substitute for those based on metallic metasurfaces generally tend to have sharper resonance curves and hence larger FOM and Q-factor due to the fact that they replace the conduction current leading to ohmic loss with low-loss displacement current [21,22]. In addition, the all-dielectric structure is capable of exciting Mie resonances including electric and magnetic dipoles [23]. These features offer new opportunities for achieving high-performance refractive index sensors.

In sensing applications, extremely narrow linewidths represent the ability to detect slight frequency shifts, so high-Q-factor resonance is desired [24]. The theory of bound state in the continuum (BIC) has recently been used to achieve resonances with high Q-factors. BICs are nonradiative states with completely confined radiation pathways in the continuous spectrum [25], which exist in lossless structures as an idealization of infinite Q-factor and zero linewidth [26–28]. In fact, BIC can be transformed into leaky resonance by introducing a defect that

* Corresponding authors at: Center for Advanced Optoelectronic Functional Materials Research and Key Laboratory of UV Light-Emitting Materials and Technology of Ministry of Education, College of Physics, Northeast Normal University, Changchun 130024, China (Z. Liang).
E-mail addresses: liangzz@nenu.edu.cn (Z. Liang), djmeng@sklao.ac.cn (D. Meng).

https://doi.org/10.1016/j.rinp.2021.105125
Received 26 October 2021; Received in revised form 7 December 2021; Accepted 12 December 2021
Available online 14 December 2021
2211-3797/

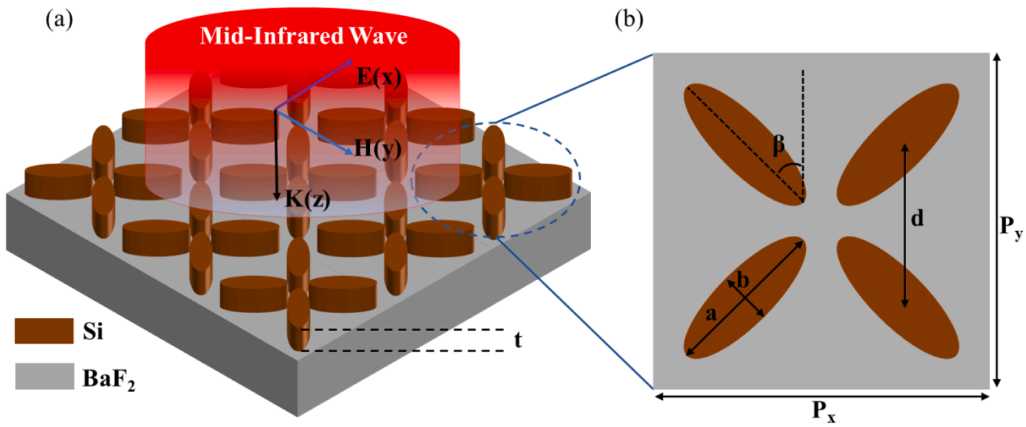

Fig. 1. (a) schematic of the silicon tetrameric clusters array metasurface structure. (b) top view of the unit cell and the geometric parameters. The geometric parameters are $P_x = P_y = P = 4.5$ μm, $\beta = 45°$, $a = 2.2$ μm, $b = 0.54$ μm, $t = 2$ μm.

destroys the structural symmetry [29], thereby obtaining a finite high Q-factor and an extremely narrow resonance linewidth. This mechanism of transforming BIC can effectively improve the quality factor of resonance and enhance the electromagnetic field [30], which will contribute to the sensing applications [31]. Some recently reported narrow linewidth resonances generated by various metasurfaces have been revealed to arise from distortion of the symmetry-protected bound state in the continuum [32]. For example, Zhang et al. proposed a sensor based on periodic silicon pairs of rods [33], which achieved a Q-factor of up to 10^5 by manufacturing the width difference of the rods to break the symmetry. Wang et al. [24] broke the symmetry of the structure by reducing or increasing the distance between the cylinders in the cylindrical tetramer cluster, resulting in perturbations and thus obtaining high-quality resonance in the terahertz band. However, such defects and perturbations breaking the structural symmetries make the metasurface sensitive to the polarization of the incident light. It is challenging to develop high-performance RI sensors with polarization-insensitive characteristics by using QBIC resonance arising from all-dielectric metasurfaces.

Here, we propose a high-performance dual-band polarization-insensitive RI sensor based on an all-dielectric metasurface where each unit cell comprises four silicon elliptical nanodisks on BaF_2. By elaborately arranging two pairs of asymmetric silicon elliptical nanodisks forming a fourfold symmetric cluster, the metasurface acquires the property of being insensitive to the polarization of the incident light. The physical mechanism of dual-band response of the proposed all-dielectric metasurface are revealed by analyzing the distributions of electromagnetic field. In this design, two QBICs with low radiative loss are excited [32,34] and tailored for RI sensing in the mid-infrared region, including an electric dipole QBIC (ED-QBIC) and a magnetic dipole QBIC (MD-QBIC). Two sharp peaks with the full width at half-maximum (FWHM) of 3.36 nm and 4.53 nm are generated in the reflection spectrum. This dual-band response can detect more information than single-band and thus improve the capability of sensing. Refractive index sensitivity tests show that the sensitivities can reach 2756.67 nm/RIU and 2319.93 nm/RIU, the corresponding FOM values are 820.44 RIU^{-1} and 532.09 RIU^{-1}, and the Q-factors are 1916.80 and 1636.16, respectively. These results are quite competitive compared to the performance of the previous reported sensors. Our research provides a practical approach for developing polarization-insensitive high-performance RI sensors based on all-dielectric metasurfaces.

Design and methods

The schematic diagram of the tetrameric periodic array combining two pairs of asymmetric structures is given in Fig. 1(a). Each unit cell comprises four silicon elliptical nanodisks on a BaF_2 (n = 1.43)

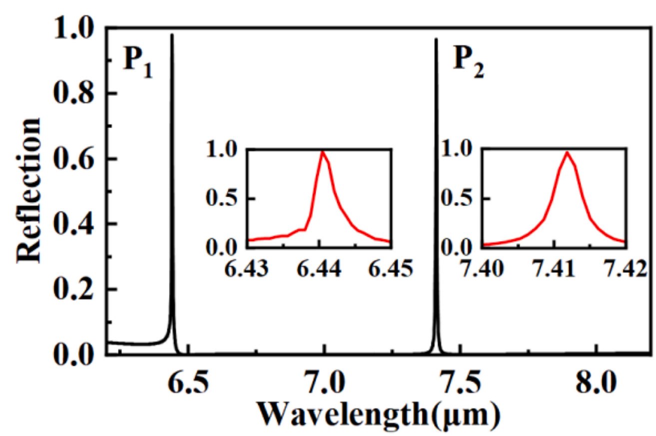

Fig. 2. The reflection spectrum of the proposed structure. The insets are the larger versions of the resonances. The surrounding medium is water (n = 1.333).

substrate. Silicon was selected as the material for the elliptical nanodisks because of its wide range of applications and ease of integration into optoelectronic devices. The optical constant of silicon is taken from Ref. [35]. The geometric parameters of the unit cell are presented in Fig. 1(b). The lattice constants P_x in the × direction and P_y in the y direction are both set to $P = 4.5$ μm. The values of the long axis a and short axis b of the elliptical nanodisks are set to $a = 2.2$ μm and $b = 0.54$ μm. The parameter t represents the height of the elliptical nanodisks and is set to $t = 2$ μm, and the parameter d represents the center distance between adjacent nanodisks and is set to $d = 2$ um. The configuration of each silicon elliptical nanodisk is characterized by a rotation angle β between the long axis and y-axis, with β set to 45°, which allows for symmetry breaking within the group of two non-parallel elliptical nanodisks while imparting fourfold symmetry to the whole metasurface.

We used Finite-difference time-domain (FDTD) method to simulate the electromagnetic properties and reflection spectral responses of this designed metasurface structure with periodic boundary conditions in the x and y directions and a perfectly matching layer in the z direction. The light source is an x-polarized plane wave incident on the metasurface along the negative z direction, as shown in Fig. 1(a).

Results and discussion

The dual-band reflection spectrum evaluated with the surrounding medium being water is shown in Fig. 2, where the insets show the larger versions of the resonances. As shown in Fig. 2, two narrow near-perfect

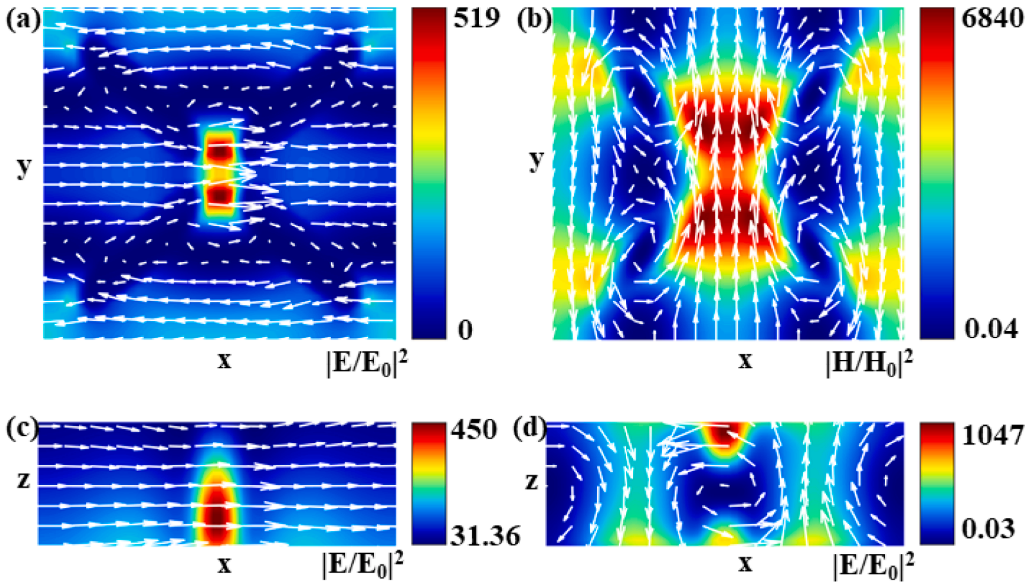

Fig. 3. (a) Electric field distribution at P_1 in the *xOy* plane. (b) Magnetic field distribution at P_2 in the *xOy* plane. Electric field distribution (c) at P_1 and (d) at P_2 in the *xOz* plane. The white arrows in (a), (c), and (d) denote the electric field vectors. The white arrows in (b) denote the magnetic field vectors.

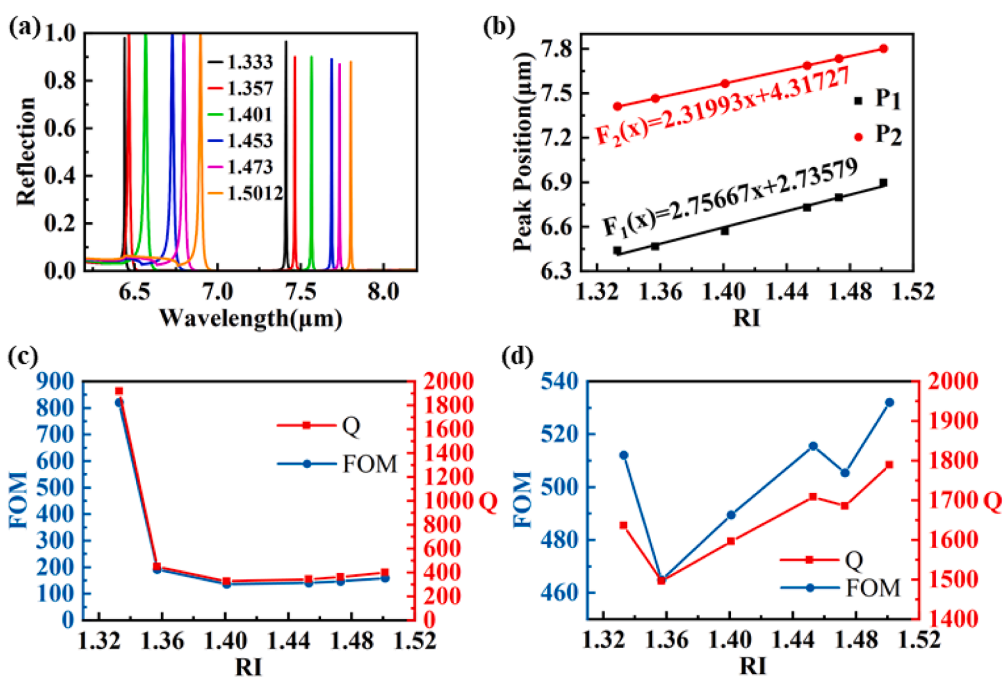

Fig. 4. (a) The reflection spectra of the proposed structure under surrounding mediums with different RI. (b) Shifts of the resonance wavelengths as a function of RI. The FOM and Q-factor of (c) peak P_1 and (d) peak P_2 versus the RI.

reflection peaks labeled P_1 and P_2 were achieved at the wavelengths of 6.44046 μm and 7.41180 μm, corresponding to reflections of 97.89% and 96.46%, respectively. The FWHMs of peaks P_1 and P_2 are 3.36 nm and 4.53 nm, whose quality (Q) -factors are as high as 1916.80 and 1636.16 respectively (The Q-factor is equal to the ratio of the resonant wavelength to the FWHM of the resonant peak). These properties enable the proposed all-dielectric metasurface structure to have good performance in sensing.

To gain further insight into the properties of supported quasi-BIC resonances, we investigated the distributions of electromagnetic field for TM mode at each resonance peak. Fig. 3(a) and (b) show the electric field distribution at P_1 and the magnetic field distribution at P_2 in the *xOy* plane, while Fig. 3(c) and (d) illustrate the distribution of the corresponding electric field vectors in the *xOz* plane. Electric field vectors in the *xOz* plane in Fig. 3(c) are linearly along the *x*-axis, thus indicating the properties of electric dipole (ED) at P_1. And the electric field vectors in the *xOz* plane in Fig. 3(d) form a loop which indicates the magnetic dipole (MD) nature at P_2. The electric field intensity of the ED-QBIC resonance in Fig. 3(a) can be enhanced by a factor of approximately 519, and the magnetic field intensity of the MD-QBIC resonance in Fig. 3(b) can be enhanced by a factor of approximately 6840. In addition, the enhanced electromagnetic fields are mainly focused on the gap between the silicon elliptical nanodisks, so a higher proportion of the electromagnetic field will interact with the surrounding medium [36], which will lead to high sensitivity.

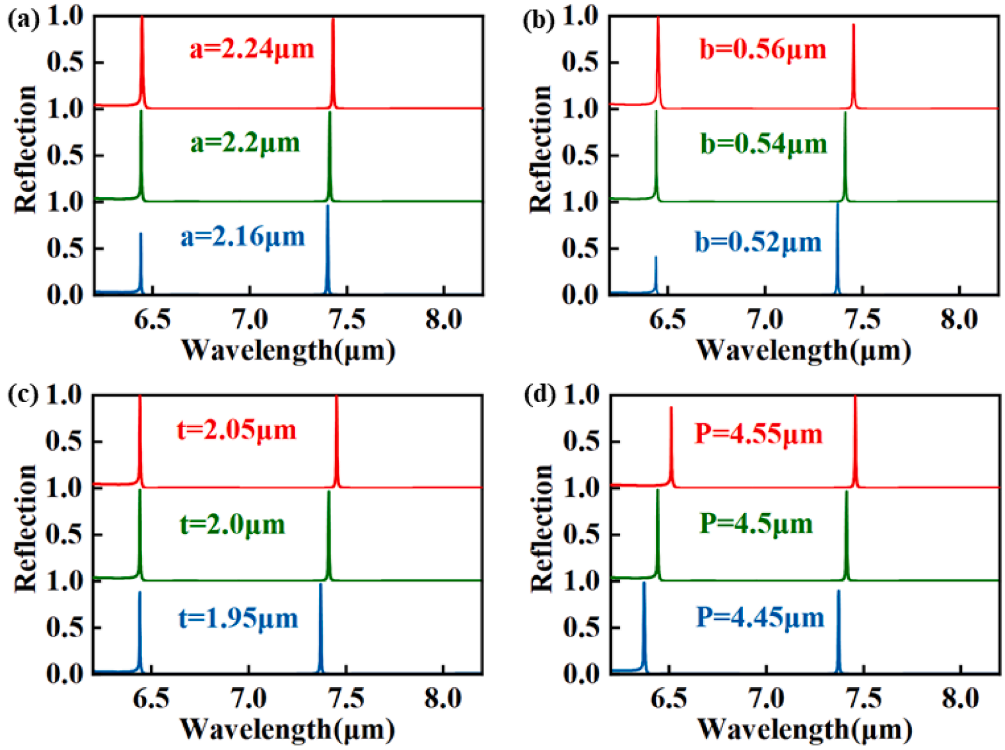

Fig. 5. Reflection spectra with different geometrical parameters: (a) long axes *a*, (b) short axes *b*, (c) thicknesses *t*, and (d) periods *P*.

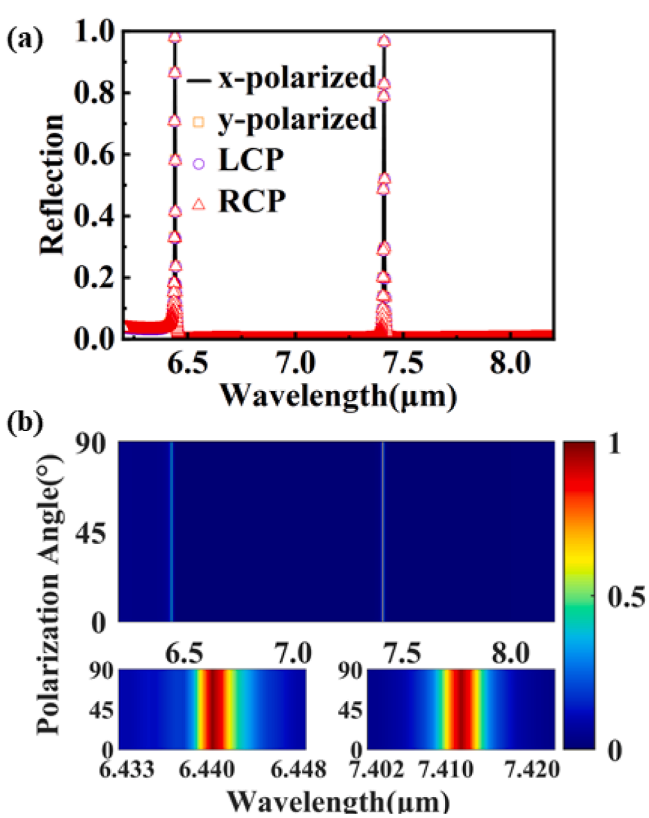

Fig. 6. (a) Reflection spectra for incident light of x-polarized (black solid curve), y-polarized (yellow squares), LCP (purple circles), and RCP (red triangles). (b) Reflection spectra with vrious polarization angles. The enlarged views near the two central wavelengths are listed below. (For interpretation of the references to colour in this figure legend, the reader is referred to the web version of this article.)

Sensitivity analysis

In general, narrower bandwidth indicates better sensing performance, thus the proposed all-dielectric metasurface structure has promising applications in RI sensing. The capability of the proposed sensor was simulated by using six different liquids surrounding mediums whose refractive index ranged from 1.333 to 1.5012. The fluids selected for testing are of high use in biochemical sensing in the medical industry, including H_2O, C_2H_6O, $C_5H_{12}O$, CCL_4, $C_3H_8O_3$, and C_6H_6. Fig. 4(a) shows the results obtained from simulation. Taking the reflection spectrum when n = 1.333 as a reference, both the reflection peaks P_1 and P_2 are significantly redshifted as the refractive index of the surrounding medium increases. Fig. 4(b) shows the relationship of the functions obtained from the linear fitting between the positions of the reflection peaks and refractive index, where the black square (red circle) line plot is linearly fitted based on the data extracted from peak P_1 (P_2) in Fig. 4(a). Two important metrics are introduced to describe and compare the performance of refractive index sensors: sensitivity (S) and figure of merit (FOM). Sensitivity is defined as the shift of the resonant peak per refractive index unit change:

$$S = \frac{\Delta\lambda}{\Delta n} \quad (1)$$

The FOM value is the ratio of sensitivity to FWHM:

$$FOM = \frac{S}{FWHM} \quad (2)$$

According to equation (1), the slopes of the linearly fitted curves in Fig. 4(b) are the sensitivities for the designed sensor.

The sensitivity, FOM, and Q-factor were calculated to characterize the sensor's performance further. It can be seen from Fig. 4(b) that the averaged sensitivities are 2756.67 nm/RIU and 2319.93 nm/RIU for peaks P_1 and P_2, respectively. Their FOM and Q-factor as the functions of the RI are shown in Fig. 4(c) and (d). The FOM and Q-factor of peak P_1 can reach up to 820.44 RIU^{-1} and 1916.80, respectively. At the same time, FOM and Q-factor decrease first and then stabilize with the

Table 1
Comparison between the reported sensors and this sensor.

Reference year	Materials	Structure	Sensitivity (nm/RIU)	Ratio (S/S_{max})	FOM (RIU^{-1})	Polarization
[18] 2010	Au	H-shaped aperture	588 (Experiment)	37.07%	3.8 (Experiment)	Sensitive
[37] 2017	Au	Double metallic nanotriangles	628	62.80%	35	Sensitive
			362 (Experiment)	29.19%	13 (Experiment)	
[38] 2018	Au	Nano-bar array micro-cavity	831	97.91%	–	Sensitive
			638 (Simulation)	96.05%		
[39] 2019	Ag	Rings dimer	470	92.82%	12	Sensitive
			570 (Simulation)	93.84%	21 (Simulation)	
[33] 2018	Si	Nanobar pairs	370 (Simulation)	37.08%	2846(Simulation)	Sensitive
[40] 2018	Si	Split ring	452 (Simulation)	42.36%	56.5(Simulation)	Sensitive
[41] 2018	Si	Glasses-shaped	433.05 (Simulation)	35.15%	116.7(Simulation)	Sensitive
[42] 2020	TiO_2	Cylinder nanodisk	786.33(Simulation)	96.16%	732(Simulation)	Insensitive
		Square nanodisk	798.5(Simulation)	97.78%	646(Simulation)	Insensitive
		Ellipse nanodisk	790(Simulation)	95.82%	540(Simulation)	Sensitive
[43] 2021	Si	Lucky knot	986(Simulation)	13.51%	32.7(Simulation)	Insensitive
[44] 2021	Ag + SiO_2	Nanoring array cavity	693.9	97.95%	119.7	Insensitive
			985.6 (Simulation)	95.64%	119.0 (Simulation)	
This work	Si	Elliptical nanodisk tetramer	2756.67	57.06%	820.44	Insensitive
			2319.93 (Simulation)	41.72%	532.09 (Simulation)	

increase of RI, as shown in Fig. 4(c). In Fig. 4(d), the FOM and Q-factor for peak P_2 show an approximately upward trend with the increase of the refractive index, whose maximum values are 532.09 RIU^{-1} and 1789.48, respectively. These results are quite competitive compared to the performance of the previous reported sensors.

Structural parameters analysis

Fig. 5 illustrates how the reflection spectrum is affected when the geometrical parameters of the structure are changed. The effect of the long axis a and the short axis b on the resonant peaks are exhibited in Fig. 5(a) and (b). With the increase of a and b, the electric field intensity at the peak P_1 increases, which manifests as a significant increase in reflection intensity, while the change of its resonant wavelength position is almost negligible. But it is the resonant wavelength position rather than the reflection intensity that changes more clearly for the peak P_2. As for the thickness t of the silicon elliptical nanodisks, during the increase of t from 1.95 μm to 2.05 μm, the parallel electric field vectors in Fig. 3(c) and the electric field loops in Fig. 3(d) are expanded along the z-axis, so the peak P_2 is redshifted while the change of the peak P_1 is manifested as an increase of the reflection intensity, as shown in Fig. 5(c). The effect of the lattice constant on the reflection spectra is shown in Fig. 5(d), where both peaks of P_1 and P_2 are slightly redshifted as the lattice constant increases. These results provide a reference for the fabrication and application of the device.

Polarization dependence

The proposed structure is fourfold symmetric, so that its performance remains constant regardless of whether it is irradiated with x-polarized or y-polarized light. In addition, the reflection spectra also remain constant when the proposed structure is irradiated by circularly polarized light. Fig. 6(a) shows the reflection spectra for the proposed sensor when the incident light polarization states are x-polarized (black solid curve), y-polarized (yellow squares), RCP (red triangles), and LCP (purple circles), respectively. It is obvious that the reflection spectra for the proposed sensor remain unaffected for these four polarization states of the incident light. Furthermore, the reflection spectra were simulated when the polarization angle changes continuously from 0 to 90°, as shown in Fig. 6(b). We intercept a section near the two central wavelengths respectively for amplification because the bandwidths are too narrow. It is seen that the reflection spectra are almost unaffected by the change in polarization angle, which indicates that the proposed structure is insensitive to the polarization directions of incident linearly polarized light. These results demonstrate the unique polarization-insensitive characteristic of the proposed sensor.

We compare the proposed sensors with the reported sensors in various aspects in Table 1. According to Ref. [18,37–39], it can be seen that for sensors based on metals such as Au and Ag, the ohmic loss makes the FOM usually low. In contrast, for some sensors based on dielectric materials such as Si and TiO2 [33,40–44], the FOM is improved while their sensitivity is less satisfactory. Besides, considering that these designs have different resonant wavelength ranges, concentrating in the NIR and MIR, in order to better refer to the effect of the resonant wavelength, we introduc the ratio of the sensitivity to the maximum differential sensitivity at a given wavelength to characterize the sensor efficiency. The maximum differential sensitivity around an isolated spectrum is given by $S_{max} = \lambda/n$ [45], based on which we approximated and compared the efficiency of each sensor. It can be seen that the efficiency of the two resonance peaks of our designed sensor reaches ~ 57.06% and ~ 41.72%, which is an improvement compared to the previous MIR sensor with an efficiency of ~ 13.51%[43] but is lower than some NIR sensors[38,39,42,44], the highest of which reaches ~ 97.95%. Consequently, the sensor we designed has a high sensitivity value, but there is still potential for improvement to approach the maximum differential sensitivity. In addition, most of the reported sensors are sensitive to incident light polarization, which will cause inconvenience to practical measurements. The structure we designed not only has the characteristic of being insensitive to incident light polarization, but also maintains high values of sensitivity and FOM, thus making it more suitable for sensors requiring high overall performance.

Conclusion

In conclusion, we have demonstrated a dual-band high-performance polarization-insensitive sensor based on an all-dielectric metasurface by elaborately arranging two pairs of asymmetric silicon elliptical nanodisks forming a fourfold-symmetric cluster. The sensor has two reflection peaks with FWHMs of 3.36 nm and 4.53 nm originating from the QBIC resonances, corresponding to quality factors of 1916.80 and 1789.48. The performance of the proposed sensor was numerically evaluated by immersing it in the surrounding mediums of six different refractive index liquids. By analyzing the reflection spectra, the maximum sensitivity and FOM were calculated to be 2756.67 nm/RIU and 820.44 RIU^{-1}. The slight shifts of the reflection spectra with respect to the structural parameters exhibit the tolerant property to fabrication errors for the proposed sensor, which provide a reference for the fabrication and application of the device. The sensor efficiency was investigated by introducing the ratio of sensitivity to the maximum differential sensitivity at a given wavelength, and the efficiencies of the two resonance peaks are ∼ 57.06% and ∼ 41.72%. In addition, the proposed sensor maintains polarization-insensitive whether it is illuminated by linearly polarized light whose polarization angle varies continuously from 0 to $\pi/2$, or by LCP and RCP light. We theoretically demonstrate that this combination between asymmetric structures is capable of achieving polarization-insensitive properties, providing a new design strategy for polarization-independent devices. This metasurface structure can play a role in sensing applications in agriculture, biomedicine, food science, and the chemical industry.

Funding

National Natural Science Foundation of China (61735018, 61805242); Jilin Scientific and Technological Development Program (20190103014JH); Excellent Member of Youth Innovation Promotion Association of the Chinese Academy of Sciences (2014193, Y201836); Leading Talents and Team Project of Scientific and Technological Innovation for Young and Middle-aged Groups in Jilin Province (20190101012JH); CAS President's International Fellowship Initiative (PIFI).

CRediT authorship contribution statement

Wenjun Liu: Conceptualization, Methodology, Software, Formal analysis, Writing – original draft. **Zhongzhu Liang:** Resources, Writing – review & editing, Supervision, Funding acquisition. **Zheng Qin:** Investigation. **Xiaoyan Shi:** Data curation. **Fuming Yang:** Software. **Dejia Meng:** Project administration.

Declaration of Competing Interest

The authors declare that they have no known competing financial interests or personal relationships that could have appeared to influence the work reported in this paper.

References

[1] Deng L, Deng J, Guan Z, Tao J, Chen Y, Yang Y, et al. Malus-metasurface-assisted polarization multiplexing. Light-Sci Appl 2020;9(1). https://doi.org/10.1038/s41377-020-0327-7.
[2] Qin Z, Meng D, Yang F, Shi X, Liang Z, Xu H, et al. Broadband long-wave infrared metamaterial absorber based on single-sized cut-wire resonators. Opt Express 2021;29(13):20275. https://doi.org/10.1364/OE.430068.
[3] Liu M, Zhu W, Huo P, Feng L, Song M, Zhang C, et al. Multifunctional metasurfaces enabled by simultaneous and independent control of phase and amplitude for orthogonal polarization states. Light-Sci Appl 2021;10(1). https://doi.org/10.1038/s41377-021-00552-3.
[4] Yin X, Steinle T, Huang L, Taubner T, Wuttig M, Zentgraf T, Giessen H. Beam switching and bifocal zoom lensing using active plasmonic metasurfaces. Light Sci Appl 2017;6(7). https://doi.org/10.1038/lsa.2017.16.
[5] Zhang C, Divitt S, Fan Q, Zhu W, Agrawal A, Lu Y, et al. Low-loss metasurface optics down to the deep ultraviolet region. Light-Sci Appl 2020;9(1). https://doi.org/10.1038/s41377-020-0287-y.
[6] Kwon H, Sounas D, Cordaro A, Polman A, Alu A. Nonlocal metasurfaces for optical signal processing. Phys Rev Lett 2018;121(17):173004. https://doi.org/10.1103/PhysRevLett.121.173004.
[7] Li L, Shuang Y, Ma Q, Li H, Zhao H, Wei M, Liu C, Hao C, Qiu CW, Cui TJ. Intelligent metasurface imager and recognizer. Light Sci Appl 2019;8:97. https://doi.org/10.1038/s41377-019-0209-z.
[8] Sain B, Zentgraf T. Metasurfaces help lasers to mode-lock. Light-Sci Appl 2020;9(1):3. https://doi.org/10.1038/s41377-020-0312-1.
[9] Lee GY, Hong JY, Hwang S, Moon S, Kang H, Jeon S, Kim H, Jeong JH, Lee B. Metasurface eyepiece for augmented reality. Nat Commun 2018;9:4562. https://doi.org/10.1038/s41467-018-07011-5.
[10] Xuan Z, Li J, Liu Q, Yi F, Wang S, Lu W. Artificial structural colors and applications. Innovation 2021;2(1):100081. https://doi.org/10.1016/j.xinn.2021.100081.
[11] Yang G, White IM, Fan X. An opto-fluidic ring resonator biosensor for the detection of organophosphorus pesticides. Sens Actuat B 2008;133(1):105–12. https://doi.org/10.1016/j.snb.2008.02.004.
[12] Yesilkoy F, Terborg RA, Pello J, Belushkin AA, Jahani Y, Pruneri V, Altug H. Phase-sensitive plasmonic biosensor using a portable and large field-of-view interferometric microarray imager. Light Sci Appl 2018;7:17152. https://doi.org/10.1038/lsa.2017.152.
[13] Tan X, Zhang H, Li J, Wan H, Guo Q, Zhu H, et al. Non-dispersive infrared multi-gas sensing via nanoantenna integrated narrowband detectors. Nat Commun 2020;11(1). https://doi.org/10.1038/s41467-020-19085-1.
[14] Camacho-Morales R, Xu L, Dimitrov N, Stoyanov L, Ma Z, Dreischuh AA, et al. Infrared upconversion imaging in nonlinear metasurfaces. Adv Photon 2021;3(03). https://doi.org/10.1117/1.AP.3.3.036002.
[15] Homola J, Yee SS, Gauglitz G. Surface plasmon resonance sensors: review. Sens Actuator B-Chem 1999;54(1–2):3–15. https://doi.org/10.1016/s0925-4005(98)00321-9.
[16] Haes AJ, Van Duyne RP. A unified view of propagating and localized surface plasmon resonance biosensors. Anal Bioanal Chem 2004;379(7–8):920–30. https://doi.org/10.1007/s00216-004-2708-9.
[17] Cong S, Liu X, Jiang Y, Zhang W, Zhao Z. Surface enhanced raman scattering revealed by interfacial charge-transfer transitions. Innovation 2020;1(3):100051. https://doi.org/10.1016/j.xinn.2020.100051.
[18] Liu Na, Weiss T, Mesch M, Langguth L, Eigenthaler U, Hirscher M, et al. Planar metamaterial analogue of electromagnetically induced transparency for plasmonic sensing. Nano Lett 2010;10(4):1103–7. https://doi.org/10.1021/nl902621d.
[19] Cheng Y, Zhang H, Mao XS, Gong R. Dual-band plasmonic perfect absorber based on all-metal nanostructure for refractive index sensing application. Materials Letters 2018;219:123–6. https://doi.org/10.1016/j.matlet.2018.02.078.
[20] Mahmoudi M, Lohse SE, Murphy CJ, Fathizadeh A, Montazeri A, Suslick KS. Variation of protein corona composition of gold nanoparticles following plasmonic heating. Nano Lett 2014;14(1):6–12. https://doi.org/10.1021/nl403419e.
[21] Ahmadi A, Mosallaei H. Physical configuration and performance modeling of all-dielectric metamaterials. Phys Rev B 2008;77(4). https://doi.org/10.1103/PhysRevB.77.045104.
[22] Peng L, Ran L, Chen H, Zhang H, Kong JA, Grzegorczyk TM. Experimental observation of left-handed behavior in an array of standard dielectric resonators. Phys Rev Lett 2007;98(15):157403. https://doi.org/10.1103/PhysRevLett.98.157403.
[23] Zhao Q, Zhou J, Zhang FL, Lippens D. Mie resonance-based dielectric metamaterials. Mater Today 2009;12(12):60–9. https://doi.org/10.1016/s1369-7021(09)70318-9.
[24] Wang Y, Han Z, Du Y, Qin J. Ultrasensitive terahertz sensing with high-Q toroidal dipole resonance governed by bound states in the continuum in all-dielectric metasurface. Nanophotonics 2021;10(4):1295–307. https://doi.org/10.1515/nanoph-2020-0582.
[25] Tan TC, Srivastava YK, Ako RT, Wang W, Bhaskaran M, Sriram S, et al. Active control of nanodielectric-induced THz quasi-BIC in flexible metasurfaces: a platform for modulation and sensing. Adv Mater 2021;33(27):2100836. https://doi.org/10.1002/adma.v33.2710.1002/adma.202100836.
[26] Ndangali RF, Shabanov SV. Electromagnetic bound states in the radiation continuum for periodic double arrays of subwavelength dielectric cylinders. J Mathemat Phys 2010;51(10):102901. https://doi.org/10.1063/1.3486358.
[27] Hsu CW, Zhen Bo, Lee J, Chua S-L, Johnson SG, Joannopoulos JD, et al. Observation of trapped light within the radiation continuum. Nature 2013;499(7457):188–91. https://doi.org/10.1038/nature12289.
[28] Monticone F, Alù A. Embedded photonic eigenvalues in 3D nanostructures. Phys Rev Lett 2014;112(21). https://doi.org/10.1103/PhysRevLett.112.213903.
[29] Koshelev K, Favraud G, Bogdanov A, Kivshar Y, Fratalocchi A. Nonradiating photonics with resonant dielectric nanostructures. Nanophotonics 2019;8(5):725–45. https://doi.org/10.1515/nanoph-2019-0024.
[30] Cong L, Singh R. Symmetry-protected dual bound states in the continuum in metamaterials. Adv Opt Mater 2019:1900383. https://doi.org/10.1002/adom.201900383.
[31] Srivastava YK, Ako RT, Gupta M, Bhaskaran M, Sriram S, Singh R. Terahertz sensing of 7 nm dielectric film with bound states in the continuum metasurfaces. Appl Phys Lett 2019;115(15):151105. https://doi.org/10.1063/1.5110383.
[32] Koshelev K, Lepeshov S, Liu M, Bogdanov A, Kivshar Y. Asymmetric metasurfaces with high-q resonances governed by bound states in the continuum. Phys Rev Lett 2018;121(19):193903. https://doi.org/10.1103/PhysRevLett.121.193903.
[33] Zhang Y, Liu W, Li Z, Li Z, Cheng H, Chen S, et al. High-quality-factor multiple Fano resonances for refractive index sensing. Opt Lett 2018;43(8):1842. https://doi.org/10.1364/OL.43.001842.
[34] Liu M, Choi D-Y. Extreme huygens' metasurfaces based on quasi-bound states in the continuum. Nano Lett 2018;18(12):8062–9. https://doi.org/10.1021/acs.nanolett.8b04774.
[35] E. J. Prucha, E. D. Palik. Handbook of optical constants of solids, vol. 1, 2, and 3. 1998.
[36] Hu J, Lang TT, Shi GH. Simultaneous measurement of refractive index and temperature based on all-dielectric metasurface. Opt Express 2017;25(13):15241–51. https://doi.org/10.1364/oe.25.015241.
[37] Yan Z, Wen X, Gu P, Zhong H, Zhan P, Chen Z, et al. Double Fano resonances in an individual metallic nanostructure for high sensing sensitivity. Nanotechnology 2017;28(47):475203. https://doi.org/10.1088/1361-6528/aa8229.
[38] Kong Y, Cao J, Qian W, Liu C, Wang S. Multiple fano resonance based optical refractive index sensor composed of micro-cavity and micro-structure. IEEE Photon J 2018;10(6):1–10. https://doi.org/10.1109/JPHOT.456399410.1109/JPHOT.2018.2881264.
[39] Liu X, Fu G, Zhan X, Liu Z. All-metal resonant metamaterials for one-, two-, three-band perfect light absorbers and sensors. Plasmonics 2018;14(4):967–71. https://doi.org/10.1007/s11468-018-0881-5.

[40] Liu G-D, Zhai X, Wang L-L, Lin Qi, Xia S-X, Luo X, et al. A high-performance refractive index sensor based on fano resonance in si split-ring metasurface. Plasmonics 2018;13(1):15–9. https://doi.org/10.1007/s11468-016-0478-9.
[41] Hu J, Lang T, Hong Z, Shen C, Shi G. Comparison of electromagnetically induced transparency performance in metallic and all-dielectric metamaterials. J Lightwave Technol 2018;36(11):2083–93. https://doi.org/10.1109/JLT.5010.1109/JLT.2018.2804336.
[42] Abbas MA, Zubair A, Riaz K, Huang W, Teng J, Mehmood MQ, et al. Engineering multimodal dielectric resonance of TiO2 based nanostructures for high-performance refractive index sensing applications. Opt Express 2020;28(16):23509. https://doi.org/10.1364/OE.397431.
[43] Zhang Y, Liang Z, Meng D, Qin Z, Fan Y, Shi X, Smith DR, Hou E. All-dielectric refractive index sensor based on Fano resonance with high sensitivity in the mid-infrared region. Results Phys 2021;24. https://doi.org/10.1016/j.rinp.2021.104129.
[44] Shen Z, Du M. High-performance refractive index sensing system based on multiple Fano resonances in polarization-insensitive metasurface with nanorings. Opt Express 2021;29(18):28287. https://doi.org/10.1364/OE.434059.
[45] Maksimov DN, Gerasimov VS, Romano S, Polyutov SP. Refractive index sensing with optical bound states in the continuum. Opt Express 2020;28(26):38907–16. https://doi.org/10.1364/oe.411749.